Phase-stable traveling waves stroboscopically matched for superresolved observation of trapped-ion dynamics

Florian Hasse ⬭, Deviprasath Palani ⬭, Robin Thomm ⬭, Ulrich Warring ⬭, and Tobias Schaetz ⬭[*]

Institut of Physics, University of Freiburg, Hermann-Herder-Strasse 3, 79104 Freiburg, Germany

In quantum technologies, it is essential to understand and exploit the interplay of light and matter. We introduce an approach creating and maintaining the coherence of four oscillators: a global microwave reference field, a polarization-gradient traveling-wave pattern of light, and the spin and motional states of a single trapped ion. Our method employs a UV light pattern capable of achieving a gigahertz-modulation bandwidth, here demonstrated in the megahertz regime, allowing for stroboscopic tracking of dynamic changes in phase space. We achieve noise floors of 1.8(2) nm for position and 8(2) zN μs for momentum observables, superresolving variations on timescales $\lesssim$ 100 ns. The implications of our findings contribute to enhancing quantum control and metrological applications.

I. INTRODUCTION

Quantum technologies are significantly enhancing control and sensing precision, e.g., by exploiting correlations, entanglement, and quantum nondemolition measurements [1–3]. For instance, gravitational-wave detection benefits from nonclassical states of light and homo- and heterodyning measurement techniques [4,5]. Complementary, mechanical oscillators excel at sensing displacements caused by feeble forces [6–10]. Trapped atomic ions have become fundamental in these explorations, offering insight into the details of underlying dynamics. Specifically, their well-isolated electronic (spin) and motional (phonon) states can be initialized, selectively coupled, and read out by high-fidelity operations [11,12]. Central to these manipulations is the interplay of light and matter, with interactions that span a wide frequency spectrum, from mega- to petahertz, permitting innovations in quantum metrology, simulation, and computation [12–14]. In this context, spatially structured light fields, with standing or traveling phase fronts, play an important role. They are realized via phase-coherent overlap of field sources, well controlled in frequency and polarization. Such alignments allow setting up a diverse range of intensity and polarization-gradient wave patterns applicable to atoms, ions, molecules, and nanoparticles [15]. Choices between different setups, such as cavities or free space, depend on the specific task, as well as its requirements for stability and controllability. On the one hand, Fabry-Pérot cavities provide highly stable phase patterns for spatial standing waves [16–19], which are even employed for entanglement operations [20], while their dynamical control is limited by cavity ring-down times, restricting fast modulations and traveling patterns. On the other hand, free-space setups permit fast operations and control of

dynamics, such as conditional displacement and squeezing via state-dependent optical dipole forces [21–29].

Trapped-ion systems have demonstrated proficiency in generating standing and traveling ("walking") wave patterns (megahertz), using both active [22,27,29] and passive stabilization methods [28]. However, the stability of faster traveling ("running") wave patterns in the gigahertz spin frame remains a challenging area, often circumvented through laserless couplings [30,31]. Advanced phase-stabilization techniques are needed to maintain stability across measurement series and synchronize multiple oscillators. This enhanced control can lead to more refined interactions with quantum systems, improving precision and minimizing disturbances in trapped-ion metrology [1–3,9,10,32–34]. Integrating concepts from diverse fields of quantum research and utilizing back-action-evading measurement strategies, where the qubit acts as a transducer, can contribute to resolving nanoscale processes with subnanosecond precision [4,5,8,35,36]. Fusion of such methods can increase spatial precision with higher timing resolution in comparison to recent complimentary demonstrations [19,37–39]. Such advancements are poised to contribute to future explorations of quantum control and of experimental analogs of intricate quantum phenomena such as cosmic inflation and Hawking radiation, allowing the study of entanglement features that are otherwise inaccessible [40,41].

In this article, we demonstrate a method for exploring trapped-ion dynamics, exploiting the active synchronization of a global microwave (gigahertz) field with a 140-nm traveling wave shaped by counterpropagating UV light (petahertz) fields. Our approach combines gigahertz-modulation bandwidth with a resolution exceeding the diffraction limit by two orders of magnitude. We perform Ramsey spectroscopy, opening and closing the interferometer via phase-coherent pulses of different oscillators. Alternatively, closing the interferometer with a stroboscopic pulse train of our traveling light pattern allows for tracking motional wave packets in phase
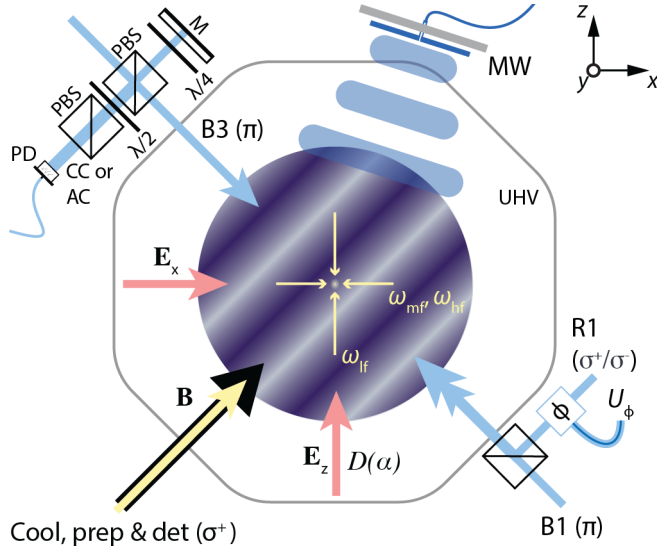
FIG. 1. Experimental setup for synchronized, coherent control and analysis of the external (motional) and internal (electronic or spin) DOFs of trapped ions (not to scale). A single ^{25}Mg$^+$ ion is spin polarized and cooled close to the motional ground state while being confined by static and radio-frequency fields. We exploit electric fields $\mathbf{E}_x$ and $\mathbf{E}_z$ (red arrows) to statically offset or coherently displace the ion in the x-z plane. We coherently control the spin state by microwave fields (MW) while we exploit two-photon stimulated-Raman (TPSR) transitions to render the spin rotation sensitive to the motional states. The corresponding laser beams, B3 and R1, are aligned in an antiparallel configuration (AC), forming a polarization-gradient traveling-wave pattern in the x-z plane. We synchronize the motional oscillator and the two spin oscillators (MW, AC) by locking the phase of the coherent displacement $D(\alpha)$ and the relative phase difference of TPSR beams to the phase of the MW. An interferometric setup for phase stabilization of the TPSR beams heterodyning the TPSR beams and mixing with the MW allows us to derive the required feedback signal U_Φ.

space (megahertz) with noise floors of 1.8(2) nm for position and 8(2) zN μs for momentum observables, respectively.

II. METHODS

Our experimental setup, as illustrated in Fig. 1 and detailed in Appendix A, integrates a linear radio-frequency ion trap with an operating frequency of $\omega_{RF}/(2\pi) \simeq 56.3$ MHz in a homogeneous magnetic quantization field of $|B| \simeq 0.58$ mT. A single ^{25}Mg$^+$ ion with nuclear spin 5/2 is selected for our study. Here, we choose the stretched states of the ground state $^2S_{1/2}$ manifold as our pseudospin (qubit) degree of freedom (DOF), i.e., $|F = 3, m_F = 3\rangle = |\downarrow\rangle$ and $|F = 2, m_F = 2\rangle = |\uparrow\rangle$, where F is the total angular momentum and m_F is the projection of the angular momentum along the magnetic-field axis, with a transition frequency of $\omega_S/(2\pi) \simeq 1.8$ GHz. The three phonon DOFs are described by three decoupled harmonic oscillators with $\omega_{LF}/(2\pi) \simeq 1.3$ MHz, the motion approximately along z (axial), and $\omega_{MF}/(2\pi) \simeq 2.9$ MHz and $\omega_{HF}/(2\pi) \simeq 4.5$ MHz, motions in the x-y (radial) plane at an angle of $\simeq 30°$ regarding the y axis. Cooling and detection lasers are tuned near a cycling transition between $S_{1/2}$ and

$P_{3/2}$ substates and are aligned with the magnetic field, as illustrated by a yellow arrow in Fig. 1. For repumping and $|\downarrow\rangle$-state preparation, we utilize beams, coupling appropriate Zeeman substates of $S_{1/2}$ and $P_{1/2}$. Fluorescence detection via a photomultiplier tube and subsequent photon histogram analysis enable us to determine the electronic-state population $P_\downarrow$, and we reconstruct population distributions of the motional states by mapping them onto the electronic states for calibration purposes [11]. Further, we use a camera to resolve ion positions within ± 1 μm in the x-z plane. All normal modes of the ion are cooled near the three-dimensional ground state with low mean thermal occupation numbers $\langle n \rangle_{th} < 0.2$. The effective size of the ion, i.e., the width of the ground-state wave functions, is $\simeq 10$ nm in all three dimensions. An arbitrary wave-form generator is employed to initialize ions near $(\Delta x, \Delta y, \Delta z) = (\Delta x_0, \Delta y_0, \Delta z_0) = (0, 0, 0)$, to reposition the ion (static displacements), and to resonantly excite motional DOFs (dynamic displacements): For static displacements, precalibrated voltage sets applied to six control electrodes shift the ion in the x-z plane. Field amplitudes are kept between $\Delta E_x = \pm 24.1$ V/m and $\Delta E_z = \pm 3.6$ V/m, corresponding to static displacements of $< \pm 200$ nm. For dynamic displacements along the axial motion, we apply a coherent excitation pulse $D(\alpha)$ via a single electrode, generating an oscillating electric field (red arrow in Fig. 1) pointing predominantly along z at ω_{LF} for fixed durations, with tunable phases and amplitudes to initialize coherent displaced states with $\alpha = |\alpha| \exp(i\vartheta_0)$, realizing a displacement operation, with tunable amplitude $|\alpha|$ and phase ϑ_0. We send a microwave (MW) reference signal via a biquad antenna to the ion to control and synchronize the spin DOF. In addition, we manipulate the electronic and motional DOFs coherently using two-photon stimulated-Raman (TPSR) transitions. We employ a 280-nm UV laser system, detuned from the $S_{1/2}$-to-$P_{3/2}$ transition by $\Delta_R/(2\pi) \simeq 20$ GHz, to apply TPSR couplings. The laser output beam is split multiple times via acousto-optic modulators (AOMs) into three individually controllable beams: B1 (π polarized), B3 (π polarized), and R1 ($\sigma^+ + \sigma^-$ polarized). The frequency difference between these beams can be fine-tuned around $\omega_S = \omega_{B1} - \omega_{R1} = \omega_{B3} - \omega_{R1}$. The collimated beams are focused using 150-mm focal-length lenses, yielding beam waists of $\simeq 50$ μm near the ion with a Rayleigh length of $\simeq 30$ mm. We utilize two distinct TPSR beam combinations: a collinear configuration (CC; with B1 and R1) with motion-insensitive couplings and an antiparallel configuration (AC; with B3 and R1) with motion-sensitive couplings to all three normal modes. The effective AC wave vector k_{AC} points along B3 towards R1, yielding a polarization-gradient traveling-wave (PGTW) pattern with a period of $\simeq 140$ nm, and is used, e.g., for sideband cooling. We establish and maintain phase coherence between AC, MW, and $D(\alpha)$ pulses via an active-phase-stabilization setup (see Appendix A). The optical components of this system are housed within a solid aluminum block approximately 20 cm^2, and individual laser beams B1, B3, and R1 are directed in free space through tubes over multiple meters, reducing disturbances from convection. We explain the AC beam path through the stabilization setup in Fig. 1: Beam R1 passing the trapping region is redirected inside a polarizing beam splitter (PBS) towards a quarter-wave ($\lambda/4$) plate onto a $0°$ mirror (M), back-reflected, and

overlapped with a fraction of the B3 beam inside the PBS. Both beams pass through a half-wave ($\lambda/2$) plate and a second PBS, matching their polarization, onto a photodiode (PD) with a gigahertz bandwidth. The remaining fraction of B3 overlaps with R1 in the trapping region, generating the traveling structured light pattern. When set to the phase-locked mode, the CC or AC beams generate heterodyne signals (gigahertz) on the PD at ω_S, and the effective TPSR phase is referenced via a homodyne mixing of this laser beat note and the MW local oscillator. A control signal U_Φ tunes a phase shifter, controlling the phase Φ of the signal that is driving our AOMs. In this way, we establish an active tuning range of $\simeq 10.4$ rad at a bandwidth of $2\pi \times 20$ kHz. The coherence of the $D(\alpha)$ pulse with the MW signal is ensured by a 10-MHz GPS-referenced master clock that synchronizes (phase references) all relevant components of our classical control and data acquisition system. Typical experimental sequences commence with an initialization section: Ion positions are set, and an optional phase *lock-up* pulse for the TPSR combinations with a duration of 100 μs is applied, followed by the preparation of motional and electronic states lasting a few milliseconds. Each sequence concludes with detecting the spin states, which takes 30 μs, and we repeat the full sequence a few hundred times at fixed parameter settings.

III. RESULTS

In an initial benchmark of our active-phase stabilization, we adopt a Ramsey-type experiment [see Fig. 2(a)] and establish the following hybrid calibration sequence: After initialization in $|\downarrow\rangle$, a spin-superposition state is generated by a MW $\pi/2$ (synchronization) pulse, and coherence is assessed via CC or AC $\pi/2$ (analysis) pulses with variable phase φ. As an example, we present raw data for an AC sequence in Fig. 2(b) with a coherence contrast of 0.76(3).

From repetitions of the hybrid calibration sequences for fixed parameters (see Appendix B), we infer short-term stability of the AC combination of 0.206(9) rad at 2 s and long-term stability of 0.38(2) rad at 40 s and 0.65(5) rad at 200 s. Similarly, for the CC combination, we record phase stabilities: 0.156(5) rad at 2 s, 0.026(1) rad at 40 s, and 0.016(2) rad at 200 s. From comparisons of such measurement runs and numerical simulations, we determine that the main stability limitation of the AC pattern stems from beam-path variations ranging from 5 to 15 nm on timescales of tens of seconds and longer. In addition, we estimate motional effects from finite mode temperatures and sizes to be negligible and determine that the stability of our AC pattern is not limited by our feedback electronics (see Appendix B). To account for residual pattern drifts, we can interleave calibration sequences to effectively reduce phase variations to $\lesssim 0.1$ rad on all relevant timescales (see Appendix B).

In the following demonstrations, we apply extensions of the Ramsey hybrid sequences with MW and AC, enabling localized spin-phase probing and control. In an initial application, we execute the Ramsey sequence with a fixed relative analysis phase of $\varphi \simeq \pi/2$ for variable Δx and Δz to examine the AC pattern. The corresponding data are presented in Fig. 2(c), demonstrating the stability of our active-phase-stabilization system. By fitting a sinusoidal model, we obtain
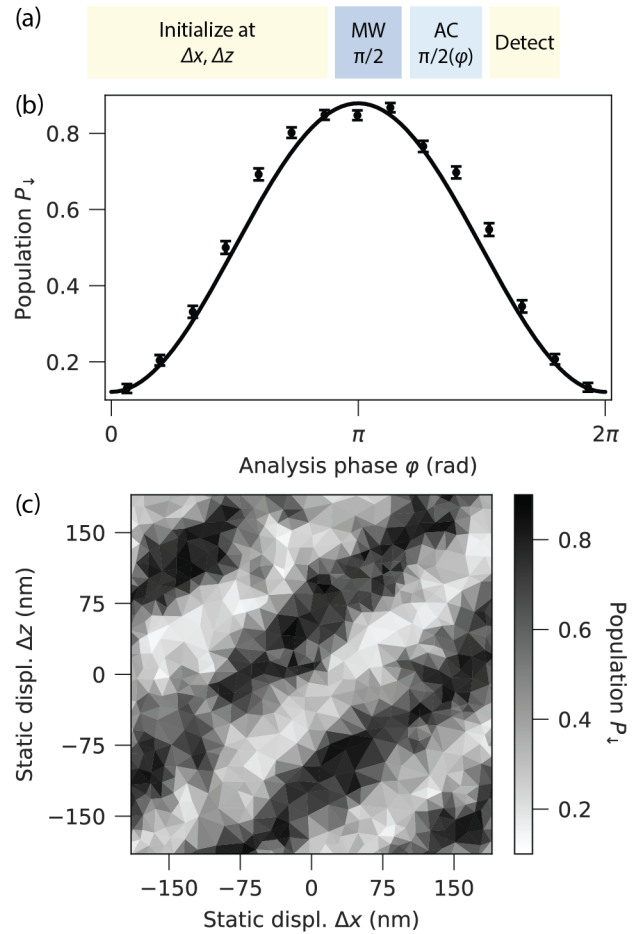

FIG. 2. Probing the phase stability of the polarization-gradient traveling-wave pattern. (a) After initialization, the spin phase is synchronized using a global MW $\pi/2$ pulse. An AC pattern providing an analysis $\pi/2$ pulse with a variable phase φ, followed by state detection of $|\downarrow\rangle$. (b) With active-phase stabilization (data points), we achieve a coherence contrast of 0.76(3), constrained by AC beampath jitters of $\simeq 10$ nm. The effects of both temperature and size on motion remain negligible. (c) We reconstruct the two-dimensional AC phase fronts in the x-z plane, signifying full-wavelength displacements along the effective wave vector.

$\lambda_{AC} = 138(1)$ nm and a pattern rotation of 0.840(7) rad in relation to the z axis, in agreement with estimates based on geometric considerations.

In an advanced application, we resolve the dynamics of coherent displaced states of the axial mode. We reconstruct expectation values of position $\langle X \rangle$ and momentum $|\langle P \rangle|$ through a back-action-evading method, leveraging stroboscopic applications of the AC pattern, with the qubit degree of freedom serving as a transducer for the repetitive measurement process. Figure 3(a) illustrates our advanced sensing sequence: We initialize displaced states with variable α via our dedicated control electrodes within fixed durations of 5 μs. We precalibrate our displacement pulses $D(\alpha)$ using conventional methods [11]. The global MW $\pi/2$ synchronization pulse is followed by a fine-tuned stroboscopic AC $\pi/2$ pulse consisting of a pulse train with 30 flashes, each of duration $\delta t \simeq 100$ ns. We calibrate and maintain a coherent pulse train
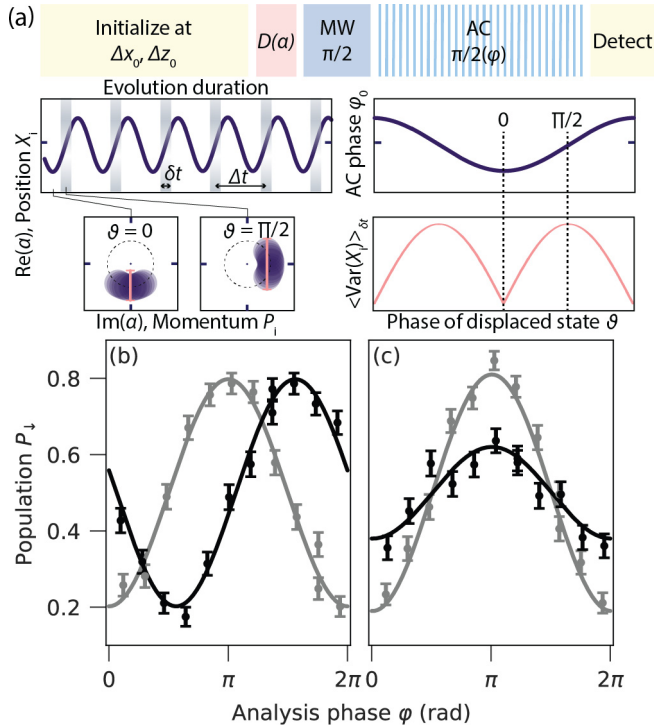
FIG. 3. Stroboscopic polarization-gradient traveling-wave pattern probing the dynamics of displaced states. (a) We initialize a single ion and apply a coherent excitation pulse $D(\alpha)$ for a fixed duration and variable phase ϑ_0 and amplitude $|\alpha|$. The sequence continues with a synchronization pulse, followed by a stroboscopic AC analysis pulse train of variable φ, and concludes with $|\downarrow\rangle$-state detection. We illustrate the trajectory of a coherently displaced state and highlight tunable pulse-train parameters: 30 flashes with duration $\delta t \simeq 100$ ns, cycle duration $\Delta t = 2\pi/\omega_{LF}$, and progressing phase to set up a complete $\pi/2$ pulse (see Appendix D). Phase-space diagram snapshots (not to scale) illustrate the time-averaged shapes of displaced states for $\vartheta = \{0, \pi/2\}$: The finite δt yields a modulation of the time-averaged variance of the ion position $\langle \text{Var}(X_i)_{\delta t} \rangle$ as a function of $\vartheta = \vartheta_0 + \omega_{LF}t$. (b) and (c) We show experimental results (data points) with model fits (solid lines) as a function of φ for sets of $|\alpha| = \{0, 6.5(2)\}$ (gray and black data points, respectively) and for $\vartheta_0 \simeq 0$ in (b) and $\vartheta_0 \simeq \pi/2$ in (c).

by precisely recording the evolving phases and regularly referencing them to the MW field. The cycling duration is set to $\Delta t = 2\pi/\omega_{LF}$. We repeat this sequence for sets of ϑ_0 and $|\alpha|$ and probe $P_\downarrow$ as a function of φ. Changes in position $\langle X \rangle$ are linearly encoded in relative analysis phase shifts φ_0, while the magnitude of momenta $|\langle P \rangle|$ are encoded nonlinearly through contrast variations ΔC due to the finite-time effects of the flashes (see Appendix D). We illustrate the underlying principle in a series of time-averaged snapshots of phase space, where the phase of the displaced state evolves as $\vartheta = \vartheta_0 + \omega_{LF}t$ but yields smeared-out shapes increasing in size $\propto |\alpha|$: For $\vartheta \simeq 0$, momenta are lowest, and the wave packet's effective size, given by the time-averaged variance of the ion position $\langle \text{Var}(X_i)_{\delta t} \rangle$, is minimal. That is, the phase of the traveling wave is well defined, the contrast is highest, and $\varphi_0 \propto |\alpha|$. Conversely, for $\vartheta \simeq \pi/2$, momenta are largest, and the time-averaged wave-packet size (in position
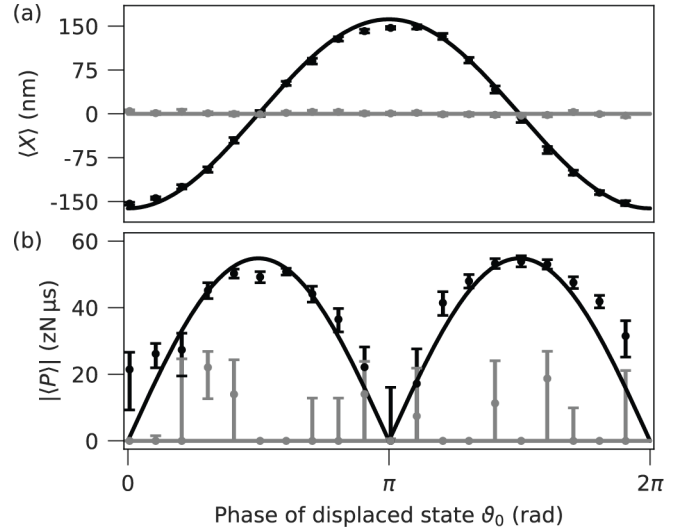

FIG. 4. Decoding of the position and momentum of coherent displaced states. (a) Position $\langle X \rangle$ and (b) the magnitude of momentum $|\langle P \rangle|$ are encoded in linear phase shifts and nonlinear contrast variations in the spin DOF, respectively. We depict corresponding expectation values of coherent displaced states of the axial motion as a function of the displacement phase ϑ_0. Two discrete amplitudes are shown: $|\alpha| = 0$ (gray) and 6.5(2) (black). Solid lines represent ideal harmonic oscillator models, and we find noise floors of 1.8(2) nm and 8(2) zN µs for position and momentum observables, respectively. In the consideration of the underlying time evolution of the displacement phase $\vartheta(t) = \vartheta_0 + \omega_{LF}t$, our method demonstrates a temporal resolution of $\lesssim 100$ ns.

space) is maximal. Consequently, the resulting averages over a larger distance yield the lowest phase-scan contrast, which is minimal for the largest $|\alpha|$. Corresponding samples of experimental results are shown in Figs. 3(b) and 3(c). We determine dedicated decoding functions from numerical predictions for our chosen parameters and apply these to two datasets of variable ϑ_0 and $|\alpha| = \{0, 6.5(2)\}$. Figure 4 shows decoded data together with coherent-displaced-state expectations that are calculated for fixed parameters (see Appendix D). We find qualitative agreement of data and idealized harmonic oscillator expectations. Noise floors are derived from the standard deviation of the dataset shown in Fig. 4 with $|\alpha| = 0$, and corresponding uncertainties are estimated with bootstrapping techniques, yielding $\simeq 1.8(2)$ nm and $\simeq 8(2)$ zN µs for position and momentum observables, respectively (see Appendix D). The sensitivity, dynamic range, and bandwidth of our sensing technique can be tuned by adjustments of the flash properties, currently limited by the speed of sound and laser beam waists in the AOMs. Numerically, we find that (1) our stroboscopic method can probe, e.g., squeezed-state dynamics and (2) the amount of back-action, the change in the motional state due to the probing, can be optimized for anticipated applications (see Appendix D). Additionally, if we selectively adjust modulation frequency and phase, our approach can be adapted to explore combinations of displaced and squeezed states, inferring individual amplitudes and phases of such superpositions.

IV. DISCUSSION

In conclusion, we actively stabilized a PGTW pattern, probing the ion's position in sync with its motion. This demonstrated a coherent link between all our control fields and ensured prolonged phase stability beyond single-shot operations. The results obtained from our prototype hybrid Ramsey sequences and additional numerical studies allow us to summarize the following key findings and indications: (1) We resolved the 140-nm light pattern with superresolution using an effective probe size of approximately 10 nm, provided by the width of the ground-state wave function of a single atom. (2) We recorded variations in position and momentum observables of the dynamics of an excited state in phase space, exemplarily demonstrated here for coherently displaced states in the megahertz regime. (3) Our technique can be adapted to (cyclic) nonclassical states, particularly squeezed states, to further increase the sensitivities of position or momentum measurements. (4) Notably, our modulated interactions can be fine-tuned either to enable minimally invasive measurements of phase-space properties or to allow for coherent, spin-phase-dependent steering of phonon excitations. Our method may benefit from quantum-clock synchronization effects, exploiting temporal correlations for enhanced measurement accuracy, as recently shown in [34]. In particular, we plan to expand our methods to transferring spatial entanglements, which are present in multimode squeezed states [40,41], into the robust electronic degrees of freedom of multiple ions. Specifically, we plan to continue the quest of studying analogs of relativistic quantum effects otherwise inaccessible to direct exploration, e.g., Hawking radiation and the physics of the early universe. Generally, our work constitutes a contribution to advanced and versatile quantum control and measurement methods.

APPENDIX A: DETAILS OF THE EXPERIMENTAL SETUP

Our trap, housed in an ultrahigh-vacuum chamber, maintains a residual gas pressure below 10^{-8} Pa. We stabilize the laboratory environment's temperature to within ± 0.3 K to mitigate unwanted thermal variations. For more details about our specific experimental methods and apparatus, we refer to [42–44], while a general introduction to trapped-ion techniques can be found in Ref. [11]. Notably, the designated manipulation periods within each sequence are shorter than any potential spin or motional dephasing durations, and from pure MW-controlled Ramsey measurements, we assess a coherence time of $\tau = 70(1)\,\mu s$ for equal spin-superposition states, constrained by magnetic-field fluctuations.

All relevant control equipment up to the gigahertz regime is actively phase locked to a 10-MHz master clock. Our Global Navigation Satellite System disciplined time and frequency
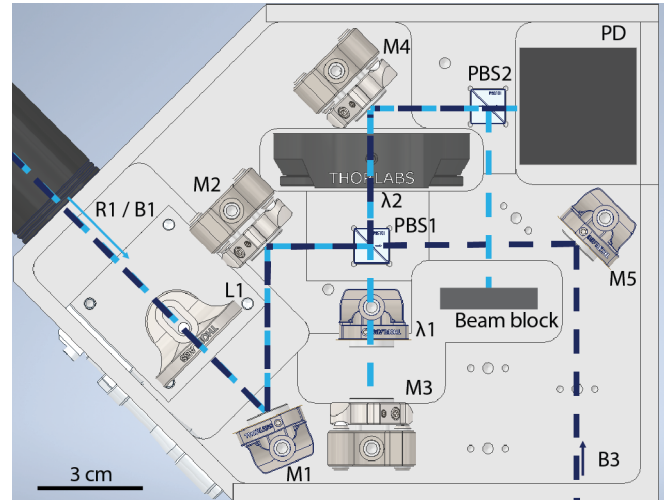

FIG. 5. Our phase-stabilization setup. The optical components are arranged within an aluminum monolithic block. Beams R1 and B1 are overlapped, aligned with the ion, and directed towards the PD, facilitating phase-referenced CC control beams. In addition, the majority of the power of beam B3 is aligned antiparallel to R1 near the ion, and a smaller fraction is overlapped with R1 on the PD, enabling phase-referenced AC control beams. The system allows for real-time switching between stabilized CC and AC beams.

reference comes with a referenced internal time base that has a phase noise of less than -125 dBc/Hz at 10-Hz offset. To ensure shot-to-shot phase coherence, we build a phase-stabilization setup to establish a phase-coherent link between the MW field and the TPSR beams. Otherwise, atom-light interaction would be randomized in between experiments [27]. Several measures are undertaken: We utilize the same direct digital synthesizer (DDS; phase referenced to the master clock) to generate the MW signal and control the AOMs of the TPSR beams, ensuring passive phase coherence. Additionally, we shield the laser beams with tubes from air disturbances. For active stabilization, we employ our phase-referencing setup detailed in the main text, with a sketch of the mechanical setup displayed in Fig. 5. To actively combine AC and MW, the PD is illuminated with approximately 1 mW from R1 and approximately 0.2 mW from B3, yielding a heterodyne signal at 1.8 GHz of approximately -60 dBm, with the noise floor at approximately -100 dBm. This signal undergoes filtering and amplification to approximately $+15$ dBm, with the noise floor at approximately -25 dBm, before homodyning with the MW signal. A resulting error signal is employed through a servo lock to alter the AOM phase of one of the TPSR beams, ensuring short- to medium-term phase coherence between AC and MW, a feature unattainable with solely passive stabilization (see the stability estimates below). Similar power levels and procedures are used for the CC beam configuration (see Fig. 5).

APPENDIX B: STABILITY ESTIMATION OF TPSR PHASE

We use the following Ramsey-type experimental sequences of pure or hybrid (MW and TPSR) control fields to estimate phase coherence:

TABLE I. Phase stability on short-term (2 s), medium-term (40 s), and long-term (200 s) scales for relevant coherent coupling-field combinations.

	Phase variance (deg)		
	2 s	40 s	200 s
MW MW	3.8(2)	1.17(6)	0.63(5)
CC CC	4.5(2)	1.15(6)	0.51(4)
AC AC	5.5(2)	1.93(9)	5.5(5)
MW CC	7.2(3)	1.49(8)	0.89(9)
MW AC	11.8(5)	22(1)	37(3)

(1) An optional lock-up (TPSR-to-MW phase referencing) pulse ($\simeq 100\,\mu s$) is emitted.

(2) Initialization occurs in the spin state $|\downarrow\rangle$ and close to the three-dimensional (3D; motional) vacuum state, with Doppler cooling ($\simeq 1530\,\mu s$) and 3D sideband cooling ($\simeq 3$–8 ms) using the AC configuration.

(3) A $\pi/2$ pulse with MW ($\simeq 5\,\mu s$) or TPSR ($\simeq 2$–3 μs) beams is emitted, synchronizing the spin phase to the MW or TPSR control field with fixed phase.

(4) Variable waiting duration (0.01 to 100 μs) is, for most experiments, set to the minimal duration, while being varied to infer coherence durations.

(5) A second $\pi/2$ pulse with MW or TPSR beams is emitted to analyze coherence, with variable phase φ or with fixed phase φ_0.

(6) In the detection step ($\simeq 30\,\mu s$), fluorescence photons are detected via the photomultiplier tube; histograms are used to infer $P_\downarrow$.

See Table I for pertinent benchmark figures for short-, medium-, and long-term stabilities. We use Allan deviations [45,46] to estimate the stability of our phase-stabilization setup. We use the experimental sequence outlined above with different combinations of MW and or TPSR beams for the synchronization and analysis pulse with a fixed analysis phase φ_0, which is chosen in a way that we detect $P_\downarrow \simeq 50\%$ at the start time t_0. We measure, for identical parameters, 500 data points for $\simeq 1100$ s. From simulations we estimate the current limitation with regard to beam-path jitter from 5 to 15 nm on timescales of tens of seconds and longer, which curtails the AC coherence, and deem motional effects from finite mode temperatures and sizes to be negligible. It is noteworthy that in all instances, we deduce a consistent coherence duration of approximately 70 μs, limited by magnetic-field fluctuations, and we can prolong these coherence durations by factors of 10 to 20 using standard strategies, i.e., spin echoes or line triggering.

Static displacements: Scanning probe of the TPSR phase fronts

In this section, we elaborate on the methodologies described in relation to Fig. 2(b) in the main text. We apply the Ramsey sequence with a combination of AC beams and a fixed phase φ_0. During initialization, we use dedicated shim fields and six control electrodes to displace the ion within the x-z plane, sampling at 670 positions using an adaptive

TABLE II. Properties of our coherent coupling fields: frequencies ω, Rabi rates Ω, effective wavelengths λ_{eff}, and corresponding Lamb-Dicke parameters η for all three motional modes.

	$\omega/(2\pi)$	$\Omega/(2\pi)$	λ_{eff}	$\eta_{\mathrm{LF}}, \eta_{\mathrm{MF}}, \eta_{\mathrm{HF}}$
	(GHz)	(MHz)		
MW	1.8	0.1	10 cm	0.00, 0.00, 0.00
CC	1.8	0.5	$\gtrsim 80\,\mu m$	0.00, 0.00, 0.00
AC	1.8	0.3	140 nm	0.40, 0.23, 0.18

technique [47] and recording $P_\downarrow$. Interleaved reference experiments monitor residual TPSR phase drifts at the origin (x_0, z_0). To realize a square scan area for Fig. 2(b), the vertices of the sampling regions are predetermined, the shim configurations are prealigned with the x and z axes, and the applied shim amplitudes are calibrated for nanometer-precision displacements. The three-dimensional data are then analyzed using a variable cosine curve, adjusting amplitude, period, phase, and rotation in the x-z plane. Fit results are given in the main text and align with our geometric expectations.

APPENDIX C: DESCRIPTIONS OF PARAMETERS AND THE TRAPPED-ION HAMILTONIAN

Our spin-motion system coupled via the TPSR polarization light pattern is described by the interaction Hamiltonian [43]:

$$
\begin{aligned}
H_{\mathrm{TI}} = {} & \hbar\omega_z \sigma_z/2 + \hbar\omega_m a^\dagger a \\
& + \hbar\Omega/2\,[C(\eta, a, a^\dagger)^\dagger \sigma_- + C(\eta, a, a^\dagger)\sigma_+].
\end{aligned} \tag{C1}
$$

The first term describes the spin, the second term represents the mode, and the third is the effective interaction engineered via our light fields. The parameters are explained as follows: $\hbar$ is Planck's constant, ω_z corresponds to the effective (dressed-state) spin frequency, and the motional mode oscillates at ω_m. The Rabi frequency Ω can be controlled by the intensity and detuning of our TPSR beams. The annihilation and creation operators of the modes are expressed as a and $a^\dagger$, while σ_- and σ_+ represent the spin system lowering and raising operators. The Pauli z operator is symbolized as σ_z. The Lamb-Dicke parameter is for our experimental parameters and the AC beam combination $\eta = \eta_{\mathrm{LF}}^{\mathrm{AC}} \simeq 0.4$ (see Table II). We introduce a generic coupling operator $C(\eta, a, a^\dagger)$, defined as $C(\eta, a, a^\dagger) = \exp[i\eta(a^\dagger + a)]$. We numerically analyze the relevant dynamics of Eq. (C1) via evaluations with QUTIP [48].

APPENDIX D: DYNAMIC DISPLACEMENTS: TRACING MOTION IN PHASE SPACE

Here, we extend our descriptions of the main text in relation to Figs. 3 and 4: After the initialization, we use $D(\alpha)$ to coherently displace the ion along the axial (LF; low frequency) mode. The analysis pulse is applied stroboscopically with fixed timing and phase shift parameters for each pulse of the train. The total duration amounts to $t_{\pi/2,\mathrm{S}} = N_\mathrm{S} \times 2\pi/\omega_{\mathrm{LF}} \simeq 30 \times 770\,\mathrm{ns} = 23.1\,\mu s$, where the number of pulses N_S is needed to yield a $\pi/2$ rotation with variable φ. In the experiments, we optimize a $\pi/2$ pulse train using a

for loop that activates the AOMs of the two TPSR beams for a duration of δt. For each pulse of the train, we iteratively readjust the phase of the DDS controlling the AOMs, incorporating calculated delays. Overall, timings and phases are optimized to effectively achieve a $\pi/2$ pulse using the experimental sequence with $\alpha = 0$.

We quantify the encoding principle via numerical simulations and illustrate exemplary results in Fig. 6. Here, we explicitly implement a time-dependent Rabi rate $\Omega = \Omega(t)$ matched to our experimental stroboscopic parameters (see explanations above). We depict spin expectation values $\langle\sigma_z\rangle$ as a function of the analysis phase φ and displaced state α parameters. In addition, we evaluate the *back action* of our stroboscopic coupling on the initial displaced state by the change in average motional quanta $\delta\langle n\rangle = \langle n\rangle_{\text{fin}} - \langle n\rangle_{\text{ini}}$. The initial $\langle n\rangle_{\text{ini}} \simeq \alpha^2$, while the final state is a nontrivial, but near-coherent, state with average quanta $\langle n\rangle_{\text{fin}}$.

To trace the ion's motional-wave-packet evolution in phase space, we require several preparatory steps and periodic recalibrations throughout the measurement series, with a focus on specialized procedures for stroboscopic measurement. Regular recalibrations involve, e.g., the qubit frequency, mode frequency, sideband cooling parameters, and initial motional quanta, along with more basic measurements such as micromotion minimization and laser beam alignment. In the measurement series, we sequentially interleave each experimental realization (approximately every 10 ms) with a phase-reference sequence with $\alpha = 0$ to re-adjust for residual AC phase variations. Figure 7 shows experimental data of $\langle\sigma_z\rangle$ for fixed $|\alpha| = 3.4(1)$ and variable φ and ϑ_0.

Figures 6(a) and 6(b) can be compared qualitatively; numerical results represent ideal-case scenarios, ignoring relevant dephasing effects.

In our analysis, we utilize numerical simulations to deduce necessary calibrations for estimating position and momentum observables from spin-projection results, as illustrated in Fig. 8. Notably, all parameters, with uncertainties around a few percent are independently measured. An independent calibration series of displacement amplitudes using red and blue sideband analysis [11] is in agreement with assumed amplitudes, considering an LF mode angle orientation of $0(5)°$ regarding the z axis.

To estimate our noise floor, the minimal resolvable signal against background noise, we use the standard deviation of data taken with $|\alpha| = 0$ (see Fig. 4 in the main text) and use bootstrapping techniques to rate the corresponding uncertainties. Bootstrapping [49–51], a statistical resampling technique, is used since the sample size is limited. It generates multiple random samples from the original data to estimate the sampling distribution of the underlying statistic, allowing us to estimate uncertainties of the calculated noise floor (standard deviation) and yielding $\simeq 1.8(2)$ nm and $\simeq 8(2)$ zN μs for position and momentum observables, respectively.

APPENDIX E: COMMENTS ON SQUEEZED STATES

In the future, the application of our stroboscopic traveling-wave pattern to squeezed states will become relevant. A squeezed vacuum state is obtained by applying the squeezing operator $S(\zeta)$ to the vacuum state $|0\rangle$. The squeezing operator
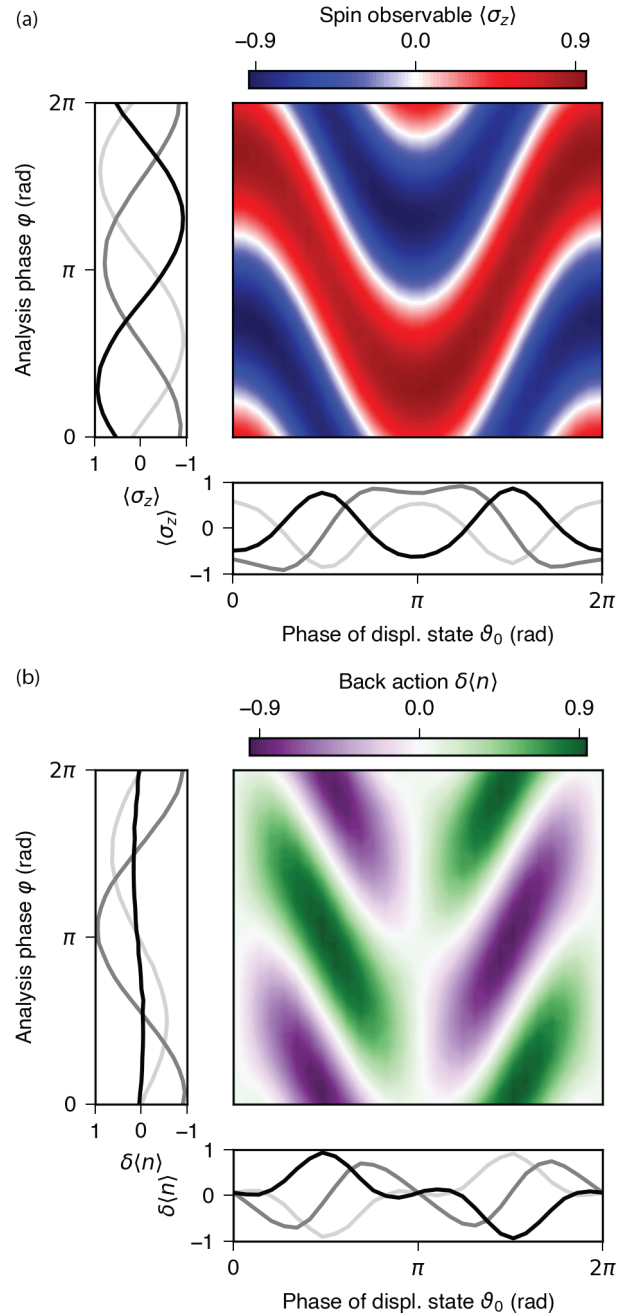

FIG. 6. Illustration of the stroboscopic measurement principle, encoding position and momentum observables in the spin observable. We perform numerical simulations to illustrate the principle of the experimental sequence (see Fig. 3 in the main text). We show (a) the detected spin observable $\langle\sigma_z\rangle$ and (b) the amount of back-action $\delta\langle n\rangle$ (900 and 600 samples, linearly interpolated) as a function of φ and ϑ_0 for fixed displacement amplitude $|\alpha| = 3$, corresponding to coherent excitation of $\langle n\rangle_{\text{coh}} = 9$. Cuts along $\vartheta_0 = \{\pi/4, \pi/2, \pi\}$ and $\varphi = \{\pi/4, \pi/2, \pi\}$ highlight the underlying effects, shown in light gray, dark gray, and black, respectively.

is defined as

$$S(\zeta) = \exp\left[\tfrac{1}{2}(\zeta^* a^2 - \zeta a^{\dagger 2})\right], \tag{E1}$$

where a and $a^\dagger$ are the annihilation and creation operators, respectively. We define the parameter $\zeta = |\zeta|e^{i\zeta_0}$, where $|\zeta|$
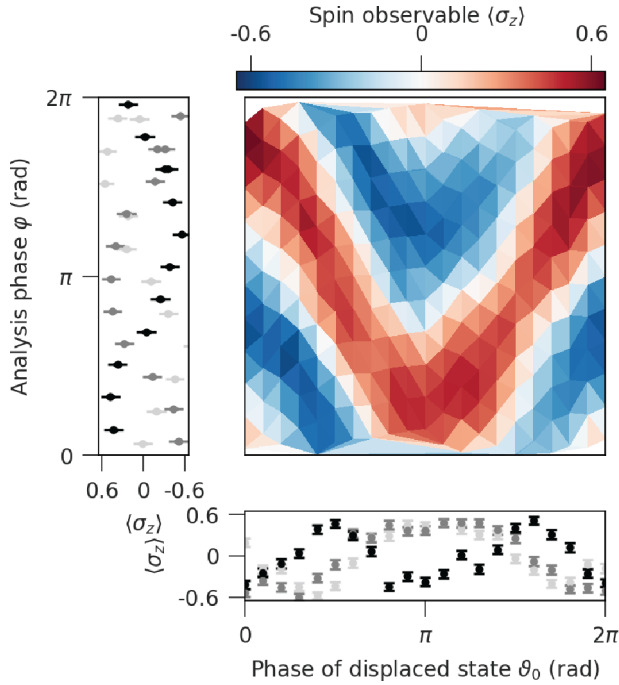
FIG. 7. Experimental raw data taken with the stroboscopic sequence [see Fig. 3(a)] for fixed $|\alpha| = 3.4(1)$ and variable φ and ϑ_0 (231 samples). In addition, we show cuts along $\vartheta_0 = \{\pi/4, \pi/2, \pi\}$ and $\varphi = \{\pi/4, \pi/2, \pi\}$ in light gray, dark gray, and black, respectively. This dataset can be compared qualitatively to numerical results shown in Fig. 6(a).

is the squeezing amplitude and ζ_0 is the squeezing phase. A squeezed vacuum state $|\zeta\rangle$ is then $|\zeta\rangle = S(\zeta)|0\rangle$. We apply a stroboscopic pulse train similar to that above, but with $\Delta t = 2\pi/(2\omega_{\mathrm{LF}})$ in our numerical code for such states, and we give some illustrations of the principles in Fig. 9. From these illustrations, we see that only contrast variations can be used to infer the squeezed-state dynamics: Squeezed positions $\zeta_0 = \pi$ yield higher contrast, and squeezed momenta $\zeta_0 = 0$ yield lower contrast than the vacuum states. The amount of
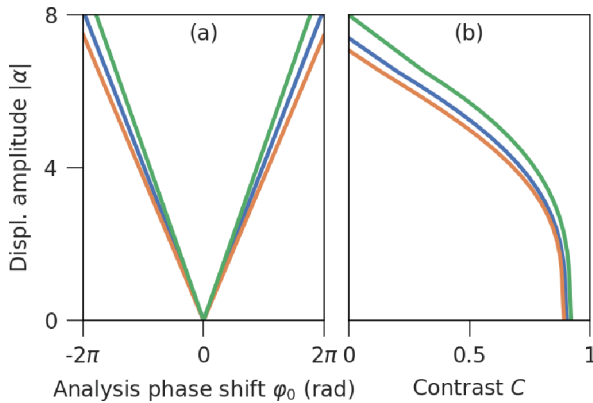

FIG. 8. Numerical calibrations to convert analysis phase shifts φ_0 and contrast C into (a) position and (b) momentum, respectively, for a single $^{25}\mathrm{Mg}^+$ ion with initial thermal $n_{\mathrm{th}} = 0.15$. To illustrate the effect of the uncertainty on the LF mode angle regarding the z axis, we show calibrations for $0°$ (blue), $-5°$ (green), and $+5°$ (orange).
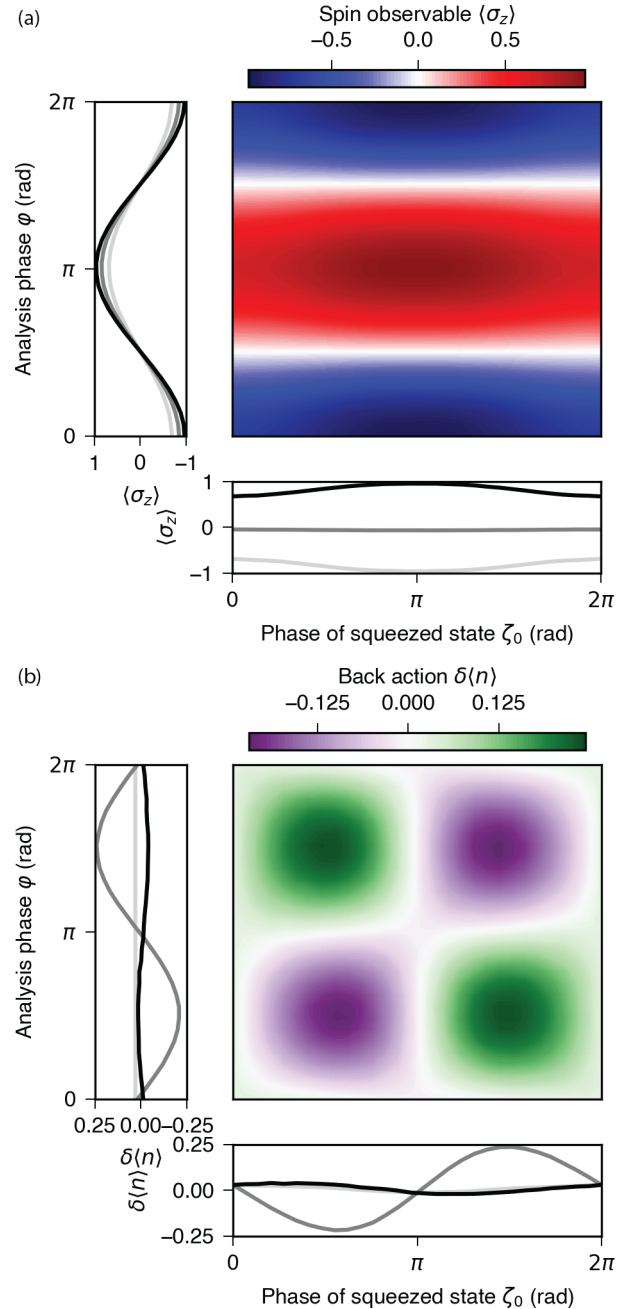

(a)

(b)

FIG. 9. Illustration of the stroboscopic control and measurement principle for squeezed states. We perform numerical simulations to illustrate the possibility of resolving and controlling squeezed-state dynamics. We show (a) the spin observable $\langle\sigma_z\rangle$ and (b) the amount of back-action $\delta\langle n\rangle$ (600 and 300 samples, linearly interpolated) as a function of φ and ζ_0 for fixed squeezing amplitude $|\zeta| = 1$ (average motional quanta $\langle n\rangle_{\mathrm{sq}} = 1$). Cuts along $\zeta_0 = \{0, \pi/2, \pi\}$ and $\varphi = \{0, \pi/2, \pi\}$ highlight the underlying effects, shown in light gray, dark gray, and black, respectively.

back-action can be tuned via the analysis and/or squeezed phase adjustments, sketching the foundation for advanced control schemes, although details need to be studied further in future work.

[1] V. B. Braginsky, Y. I. Vorontsov, and K. S. Thorne, Science **209**, 547 (1980).

[2] V. Giovannetti, S. Lloyd, and L. Maccone, Science **306**, 1330 (2004).

[3] C. L. Degen, F. Reinhard, and P. Cappellaro, Rev. Mod. Phys. **89**, 035002 (2017).

[4] J. Aasi, J. Abadie, B. P. Abbott, R. Abbott, T. D. Abbott, M. R. Abernathy, C. Adams, T. Adams, P. Addesso, R. X. Adhikari *et al.*, Nat. Photon. **7**, 613 (2013).

[5] F. Acernese *et al.* (Virgo Collaboration), Phys. Rev. Lett. **123**, 231108 (2019).

[6] R. Maiwald, D. Leibfried, J. Britton, J. C. Bergquist, G. Leuchs, and D. J. Wineland, Nat. Phys. **5**, 551 (2009).

[7] S. Knünz, M. Herrmann, V. Batteiger, G. Saathoff, T. W. Hänsch, K. Vahala, and T. Udem, Phys. Rev. Lett. **105**, 013004 (2010).

[8] M. Aspelmeyer, T. J. Kippenberg, and F. Marquardt, Rev. Mod. Phys. **86**, 1391 (2014).

[9] S. C. Burd, R. Srinivas, J. J. Bollinger, A. C. Wilson, D. J. Wineland, D. Leibfried, D. H. Slichter, and D. T. C. Allcock, Science **364**, 1163 (2019).

[10] K. A. Gilmore, M. Affolter, R. J. Lewis-Swan, D. Barberena, E. Jordan, A. M. Rey, and J. J. Bollinger, Science **373**, 673 (2021).

[11] D. Leibfried, R. Blatt, C. Monroe, and D. Wineland, Rev. Mod. Phys. **75**, 281 (2003).

[12] D. J. Wineland, Rev. Mod. Phys. **85**, 1103 (2013).

[13] I. Buluta and F. Nori, Science **326**, 108 (2009).

[14] T. D. Ladd, F. Jelezko, R. Laflamme, Y. Nakamura, C. Monroe, and J. L. O'Brien, Nature (London) **464**, 45 (2010).

[15] H. Metcalf and P. Van Der Straten, *Laser Cooling and Trapping* (Springer, Berlin, 1999).

[16] C. J. Hood, M. S. Chapman, T. W. Lynn, and H. J. Kimble, Phys. Rev. Lett. **80**, 4157 (1998).

[17] G. R. Guthoerlein, M. Keller, K. Hayasaka, W. Lange, and H. Walther, Nature (London) **414**, 49 (2001).

[18] A. B. Mundt, A. Kreuter, C. Becher, D. Leibfried, J. Eschner, F. Schmidt-Kaler, and R. Blatt, Phys. Rev. Lett. **89**, 103001 (2002).

[19] E. Deist, J. A. Gerber, Y.-H. Lu, J. Zeiher, and D. M. Stamper-Kurn, Phys. Rev. Lett. **128**, 083201 (2022).

[20] B. Casabone, A. Stute, K. Friebe, B. Brandstätter, K. Schüppert, R. Blatt, and T. E. Northup, Phys. Rev. Lett. **111**, 100505 (2013).

[21] D. Leibfried, B. DeMarco, V. Meyer, D. Lucas, M. Barrett, J. Britton, W. M. Itano, B. Jelenković, C. Langer, T. Rosenband, and D. J. Wineland, Nature (London) **422**, 412 (2003).

[22] D. B. Hume, C. W. Chou, D. R. Leibrandt, M. J. Thorpe, D. J. Wineland, and T. Rosenband, Phys. Rev. Lett. **107**, 243902 (2011).

[23] L. Karpa, A. Bylinskii, D. Gangloff, M. Cetina, and V. Vuletić, Phys. Rev. Lett. **111**, 163002 (2013).

[24] J. A. Miles, Z. J. Simmons, and D. D. Yavuz, Phys. Rev. X **3**, 031014 (2013).

[25] M. Enderlein, T. Huber, C. Schneider, and T. Schaetz, Phys. Rev. Lett. **109**, 233004 (2012).

[26] C. T. Schmiegelow, H. Kaufmann, T. Ruster, J. Schulz, V. Kaushal, M. Hettrich, F. Schmidt-Kaler, and U. G. Poschinger, Phys. Rev. Lett. **116**, 033002 (2016).

[27] M. Affolter, K. A. Gilmore, J. E. Jordan, and J. J. Bollinger, Phys. Rev. A **102**, 052609 (2020).

[28] A. R. Vasquez, C. Mordini, C. Vernière, M. Stadler, M. Malinowski, C. Zhang, D. Kienzler, K. K. Mehta, and J. P. Home, Phys. Rev. Lett. **130**, 133201 (2023).

[29] S. Saner, O. Băzăvan, M. Minder, P. Drmota, D. J. Webb, G. Araneda, R. Srinivas, D. M. Lucas, and C. J. Ballance, Phys. Rev. Lett. **131**, 220601 (2023).

[30] C. Ospelkaus, U. Warring, Y. Colombe, K. R. Brown, J. M. Amini, D. Leibfried, and D. J. Wineland, Nature (London) **476**, 181 (2011).

[31] R. Srinivas, S. C. Burd, H. M. Knaack, R. T. Sutherland, A. Kwiatkowski, S. Glancy, E. Knill, D. J. Wineland, D. Leibfried, A. C. Wilson, D. T. C. Allcock, and D. H. Slichter, Nature (London) **597**, 209 (2021).

[32] M. de Burgh and S. D. Bartlett, Phys. Rev. A **72**, 042301 (2005).

[33] B. L. Higgins, D. W. Berry, S. D. Bartlett, H. M. Wiseman, and G. J. Pryde, Nature (London) **450**, 393 (2007).

[34] G. Higgins, S. Salim, C. Zhang, H. Parke, F. Pokorny, and M. Hennrich, New J. Phys. **23**, 123028 (2021).

[35] G. Vasilakis, H. Shen, K. Jensen, M. Balabas, D. Salart, B. Chen, and E. S. Polzik, Nat. Phys. **11**, 389 (2015).

[36] M. Brunelli, D. Malz, A. Schliesser, and A. Nunnenkamp, Phys. Rev. Res. **2**, 023241 (2020).

[37] M. Drechsler, S. Wolf, C. T. Schmiegelow, and F. Schmidt-Kaler, Phys. Rev. Lett. **127**, 143602 (2021).

[38] A. A. Pushkina, G. Maltese, J. I. Costa-Filho, P. Patel, and A. I. Lvovsky, Phys. Rev. Lett. **127**, 253602 (2021).

[39] Z. H. Qian, J. M. Cui, X. W. Luo, Y. X. Zheng, Y. F. Huang, M. Z. Ai, R. He, C. F. Li, and G. C. Guo, Phys. Rev. Lett. **127**, 263603 (2021).

[40] M. Wittemer, F. Hakelberg, P. Kiefer, J. P. Schröder, C. Fey, R. Schützhold, U. Warring, and T. Schaetz, Phys. Rev. Lett. **123**, 180502 (2019).

[41] M. Wittemer, J. P. Schröder, F. Hakelberg, P. Kiefer, C. Fey, R. Schuetzhold, U. Warring, and T. Schaetz, Philos. Trans. R. Soc. A **378**, 20190230 (2020).

[42] A. Friedenauer, F. Markert, H. Schmitz, L. Petersen, S. Kahra, M. Herrmann, T. Udem, T. Hänsch, and T. Schätz, Appl. Phys. B **84**, 371 (2006).

[43] G. Clos, D. Porras, U. Warring, and T. Schaetz, Phys. Rev. Lett. **117**, 170401 (2016).

[44] M. Wittemer, Ph.D. thesis, University of Freiburg, 2019.

[45] D. Allan, Proc. IEEE **54**, 221 (1966).

[46] W. Riley and D. Howe, *Handbook of Frequency Stability Analysis* (National Institute of Standards and Technology, Gaithersburg, MD, 2008).

[47] B. Nijholt, J. Weston, J. Hoofwijk, and A. Akhmerov, *Adaptive*: Parallel active learning of mathematical functions, Zenodo, 2019, doi:10.5281/zenodo.1182437.

[48] J. Johansson, P. Nation, and F. Nori, Comput. Phys. Commun. **184**, 1234 (2013).

[49] B. Efron and R. J. Tibshirani, *An Introduction to the Bootstrap* (Chapman and Hall/CRC, Boca Raton, FL, 1994).

[50] A. C. Davison and D. V. Hinkley, *Bootstrap Methods and Their Application*, Cambridge Series in Statistical and Probabilistic Mathematics (Cambridge University Press, Cambridge, 1997).

[51] P. H. Westfall and R. D. Wolfinger, *Resampling Methods: A Practical Guide to Data Analysis* (Wiley, New York, 1997).